Raman study of phonons in $CaMn_7O_{12}$: Effects of structural modulation and structural transition

M. N. Iliev,[1] V. G. Hadjiev,[2] M. M. Gospodinov,[3] R. P. Nikolova,[4] and M. V. Abrashev[5,6]

[1]*Texas Center for Superconductivity and Department of Physics, University of Houston, Houston, Texas 77204-5002, USA*

[2]*Texas Center for Superconductivity and Department of Mechanical Engineering, University of Houston, Houston, Texas 77204-5002, USA*

[3]*Institute of Solid State Physics, Bulgarian Academy of Sciences, 1184 Sofia, Bulgaria*

[4]*Institute of Mineralogy and Crystallography, Bulgarian Academy of Sciences, 1113 Sofia, Bulgaria*

[5]*Instituto de Física, UFRGS, Porto Alegre, 91501-970 Rio Grande do Sul, Brazil*

[6]*Faculty of Physics, University of Sofia, 1164 Sofia, Bulgaria*

(Received 28 March 2014; revised manuscript received 21 May 2014; published 5 June 2014)

Polarized Raman spectra of oriented $CaMn_7O_{12}$ single crystals have been studied in a broad temperature range (5–500 K) covering the crystallographic, ferroelectric, and magnetic transitions. From the spectra obtained at room temperature (RT) 10 out of the total 12 Raman active $6A_g + 6E_g$ modes of the trigonal $R\bar{3}$ phase have been identified and assigned to definite atomic motions in close comparison to results of lattice-dynamics modeling. With the decrease in temperature below 250 K some Raman bands split, and additional spectral features, not expected for the $R\bar{3}$ structure, arise well above the magnetic transitions near 90 and 50 K. Their appearance, however, correlates with the transformation due to incommensurate structural modulation revealed by recent x-ray and neutron-diffraction studies. As temperature increases above RT the intensity of the Raman lines strongly decreases, and entering the high-temperature $Im\bar{3}$ phase the spectrum transforms its shape to that expected for a structure with disordered Jahn-Teller distortions.

DOI: 10.1103/PhysRevB.89.214302 PACS number(s): 78.30.−j, 72.80.Ga, 78.20.Bh

I. INTRODUCTION

$CaMn_7O_{12}$ attracts considerable interest due to its complex magnetic structure and observation of strong multiferroic effects [1–6]. The high-temperature phase of $CaMn_7O_{12}$ ($T >$ 450 K) is cubic $Im\bar{3}$, but below a mixed phase region ($400 < T < 450$ K), the structure becomes rhombohedral $R\bar{3}$ with three nonequivalent Mn sites, occupied by either Mn^{3+} or Mn^{4+} cations [1]. Temperature-dependent x-ray and neutron-diffraction experiments have revealed a further appearance of structural modulation below 200 K and related magnetic modulation below 90 K [7–9]. Most papers on this material are on its magnetic and multiferroic properties, with the exception of an early preliminary report [10] on the IR absorption between 90 and 623 K. Here we present results of a detailed Raman study of oriented single crystals of $CaMn_7O_{12}$ between 5 and 500 K. At room temperature (RT) ten of the twelve $6A_g + 6E_g$ Raman-allowed modes have been observed, identified by symmetry and assigned to definite atomic motions in close comparison with results of lattice-dynamics modeling. With the decrease in temperature below 200 K, a number of new spectral features appear. Their origin and specific behavior are discussed accounting for expected effects of structural modulation on the phonon band structure and activation of otherwise Raman-forbidden phonon modes. On the other hand, with increasing temperature between 300 and 400 K, the Raman spectra decrease in intensity and above the $R\bar{3}$-$Im\bar{3}$ transition change their shapes to that expected for a strongly disordered and conducting material. These transformations are discussed in terms of Jahn-Teller (JT) disorder and valence exchange.

II. CRYSTAL GROWTH, EXPERIMENTAL DETAILS, AND DENSITY FUNCTIONAL THEORY MODELING

$CaMn_7O_{12}$ single crystals were grown by the high-temperature solution growth method in pure platinum crucibles. $CaCl_2$ (anhydrous) was used as flux. The ratio (in weight percents) between the preliminary sintered single phase $CaMn_7O_{12}$ powder and the flux was 1:2. The starting mixture was heated in air through 12 h up to 1000 °C, after that was homogenized for 48 h. The $CaMn_7O_{12}$ crystal growth was accomplished during the cooling of the molten mixture in the temperature range from 1000 °C to 770 °C (cooling speed of 1 °C/h). The cooling speed in the interval of 770 °C—room temperature was kept at 100 °C/h. The $CaMn_7O_{12}$ crystallized on the walls and the bottom of the platinum crucible in the form of cubes of typical edge dimensions of 200–300 μm. The single crystals of $CaMn_7O_{12}$ were separated from flux after boiling in acetic acid.

The single-crystal data were collected on an Agilent Diffraction SuperNovaDual four-circle diffractometer equipped with an Atlas CCD detector using mirror-monochromatized MoK radiation from a microfocus source ($\lambda = 0.7107$ Å). Data collection at RT and low temperature (LT) were performed using the same crystal sample. During the LT experiments the sample was kept at 150 and 85 K with an Oxford Instruments Cobra controller device and a nitrogen atmosphere. The determination of cell parameters, data integration, scaling, and absorption corrections were carried out using the CRYSALIS PRO program package [11]. The crystal structure was solved by direct methods using SHELXS-97 and was refined by the full matrix least-squares procedure on F^2 with SHELXL-97 [12]. It was observed that the crystal structures remain rhombohedral $R\bar{3}$ (No. 148) with a hexagonal unit cell and the LT conditions cause small variations in the unit-cell parameters: RT, $a = 10.4319(9)$, $c = 6.3846(8)$ Å; LT (150 K), $a = 10.421(2)$, $c = 6.371(3)$ Å; LT (85 K), $a = 10.4207(16)$, $c = 6.371(3)$ Å.

The rhombohedral and hexagonal unit cells of the $R\bar{3}$ structure and the cubic unit cell of the high-temperature cubic $Im\bar{3}$ phase are shown in Fig. 1. The natural pseudocubic

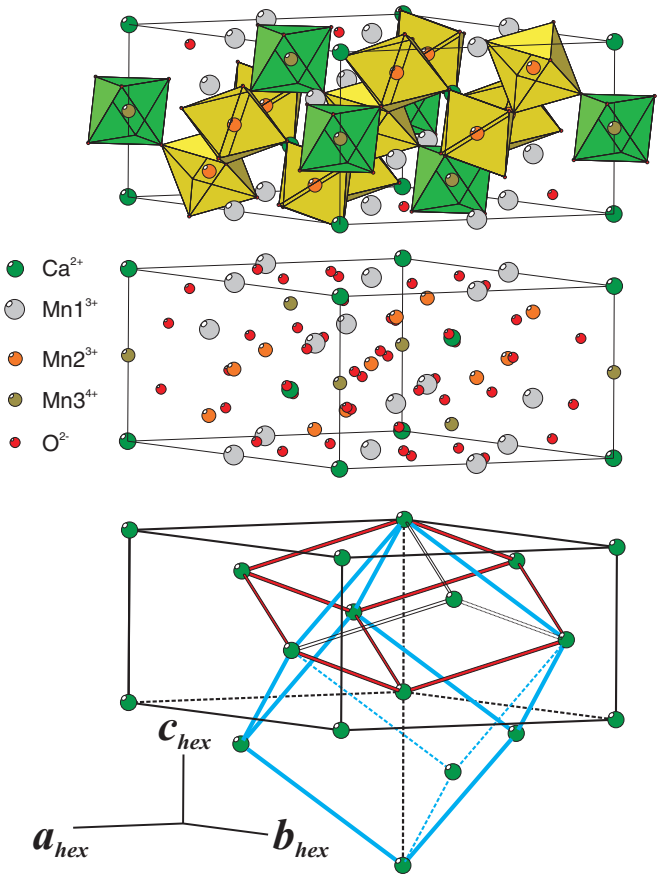

FIG. 1. (Color online) Hexagonal (black) and primitive rhombohedral (red) cells of $CaMn_7O_{12}$ (space group No. 148 $R\bar{3}$). The unit cell of the high-temperature cubic phase (space group No. 204 $Im\bar{3}$) corresponding also to the pseudocubic structure is shown in blue.

surfaces of the crystals used in the Raman experiments appear parallel to the $\{001\}$ surfaces of the $Im\bar{3}$ cell.

The Raman spectra were collected under a microscope with 633-, 515-, or 488-nm excitation using a T64000 (Horiba Jobin-Yvon) spectrometer. In low-temperature measurements the samples were cooled in an Oxford Microstat^{He} cryostat whereas for high-temperature measurements a Linkam FIR600 heating stage was used.

The lattice-dynamics calculations (LDCs) were performed within the generalized-gradient approximation of the density functional perturbation theory with the Perdew-Burke-Ernzerhof exchange-correlation functional, plane-wave basis, and norm-conserved pseudopotentials, as implemented in the QUANTUM EXPRESSO (QE) suite [13]. The electronic band structure, related properties, and LDC were calculated with the self-consistent field (SCF) method with a 70-Ry kinetic-energy cutoff for the plane waves, 280-Ry charge density cutoff, SCF tolerance better than 10^{-7}, and phonon SCF threshold of 10^{-12}. The crystal structure optimization of $CaMn_7O_{12}$ turns out to be particularly important for yielding LDC phonon frequencies deviating less than 5% from the experimental ones. As seen in Table I, the oxygen atoms occupy sites with $18f$ Wyckoff symmetry, which imposes no constraints on the value of oxygen fractional coordinates. This allows multiple oxygen configurations having crystal energy local minima. Many of these configurations, however, give large deviations in the LDC phonon frequencies. The best LDC results are obtained when the structural optimization is first performed on a fully relaxed lattice in hexagonal representation and then LDC is performed on the corresponding rhombohedral unit cell. Two types of LDC were performed. The non-spin-polarized LDC presented in this paper corresponds to the crystal in the paramagnetic (PM) state. The spin-polarized LDC in which the spins of Mn3 and Mn1 are in the same direction and opposite that of Mn2 represents our best approximation to the low-temperature spiral antiferromagnetic phase of $CaMn_7O_{12}$. We were not able to reproduce the magnetic-moment arrangement given in Ref. [5] because the QE code lacks full relativistic pseudopotentials for Mn needed for including the spin-orbit interactions in the calculations. We refer further to this electronic spin configuration in of $CaMn_7O_{12}$ as a pseudoantiferromagnetic (pAFM) state.

TABLE I. Wyckoff position and site symmetry of the atoms in the hexagonal unit cell of rhombohedral $CaMn_7O_{12}$. The irreducible representations of the Γ-point phonon modes are $\Gamma_{\text{Total}} = 6A_g + 6E_g + 14A_u + 14E_u$. Raman-active modes: $6A_g + 6E_g$; IR active modes: $13A_u + 13E_u$; acoustic modes $1A_u + 1E_u$.[a]

Atom	Wyckoff notation	Site symmetry	Irreducible representations
Ca	$3a$	S_6	$A_u + E_u$
Mn1	$9e$	C_i	$3A_u + 3E_u$
Mn2	$9d$	C_i	$3A_u + 3E_u$
Mn3	$3b$	S_6	$A_u + E_u$
O1	$18f$	C_1	$3A_g + 3A_u + 3E_g + 3E_u$
O2	$18f$	C_1	$3A_g + 3A_u + 3E_g + 3E_u$

[a] $A_g = \begin{pmatrix} a & 0 & 0 \\ 0 & a & 0 \\ 0 & 0 & b \end{pmatrix}$, $E_g = \begin{pmatrix} c & d & e \\ d & -c & f \\ e & f & 0 \end{pmatrix}$, $\begin{pmatrix} d & -c & -f \\ -c & -d & e \\ -f & e & 0 \end{pmatrix}$.

III. RESULTS AND DISCUSSION

A. Room-temperature spectra

The room-temperature spectra were obtained from the quasicubic $(001)_c$ natural crystal surface with xx, xy, $x'x'$, and $x'y'$ scattering configurations ($x \parallel [100]_c$, $y \parallel [010]_c$, $x' \parallel [110]_c$, and $y' \parallel [\bar{1}10]_c$). In these notations the first letter stands for the polarization direction of the incident radiation,

TABLE II. Polarization selection rules for the A_g and E_g modes in Raman spectra obtained from a pseudocubic (001) plane. The notations x, y, x', and y', respectively, correspond to the [100], [010], [110], and [$\bar{1}$10] quasicubic directions as x' is parallel to the X of the orthogonal XYZ coordinate system.

	A_g	E_g
$xx \equiv yy$	$\frac{1}{9}(2a+b)^2$	$\frac{4}{9}(c+\sqrt{2}f)^2 + \frac{4}{9}(d+\sqrt{2}e)^2$
xy	$\frac{1}{9}(-a+b)^2$	$\frac{1}{9}(\sqrt{2}f-2c)^2 + \frac{1}{9}(\sqrt{2}e-2d)^2$
$x'x'$	a^2	c^2+d^2
$y'y'$	$\frac{1}{9}(a+2b)^2$	$\frac{1}{9}(2\sqrt{2}f-c)^2 + \frac{1}{9}(2\sqrt{2}e-d)^2$
$x'y'$	0	$\frac{1}{3}(\sqrt{2}e+d)^2 + \frac{1}{3}(\sqrt{2}f+c)^2$

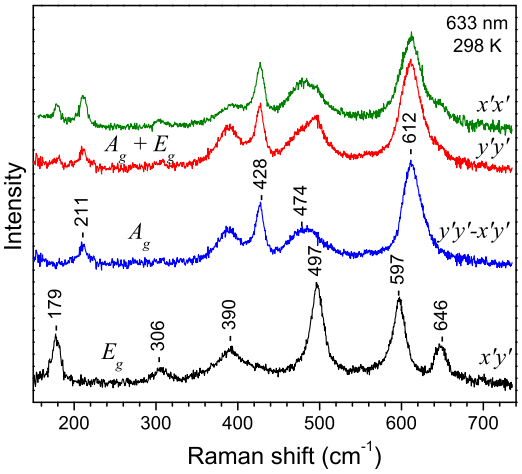

FIG. 2. (Color online) Raman spectra of $CaMn_7O_{12}$ with an $x'x'$, $y'y'$, and $x'y'$ scattering configuration. The A_g spectrum obtained by subtracting $x'y'$ from the $y'y'$ spectrum is also shown.

the second one—for the polarization of the scattered light. From symmetry configurations [14,15] one expects for the $R\bar{3}$ structure of $CaMn_7O_{12}$ $12(6A_g + 6E_g)$ Raman-active modes (Table I). The corresponding Raman tensors are given in the orthogonal coordinate system XYZ related to the hexagonal unit cell through $X \parallel \mathbf{a}_{\text{hex}} \parallel [1\bar{1}0]_c$ and $Z \parallel \mathbf{c}_{\text{hex}} \parallel [111]_c$.

The polarization selection rules for the Raman spectra from a quasicubic $(001)_c$ plane are given in Table II. The assignment of observed Raman lines to modes of A_g or E_g can be performed by comparison of the $x'y'$ and $x'x'$ spectra. Although only E_g modes are allowed with $x'y'$, both A_g and E_g are allowed with $x'x'$, $y'y'$, xx, and yy scattering configurations.

Figure 2 shows the $x'x'$, $y'y'$, and $x'y'$ spectra of $CaMn_7O_{12}$ as obtained with 633-nm excitation at room temperature. All six Raman-allowed modes of E_g symmetry are readily identified from the $x'y'$ spectra at 179, 306, 390, 497, 597, and 646 cm^{-1}. The lines at 211, 428, 474, and 612 cm^{-1} are observed only in the $x'x'$ and $y'y'$ spectra and are clearly of A_g symmetry. A comparison of experimentally observed frequencies with those predicted by lattice-dynamics modeling are given in Table III.

TABLE III. Comparison of experimentally observed and LDC-predicted frequencies (in cm^{-1}) for the A_g and E_g modes in $CaMn_7O_{12}$.

Mode	Expt.	LDC PM	LDC pAFM	Mode	Expt.	LDC PM	LDC pAFM
$A_g(1)$	211	211	215	$E_g(1)$	179	176	211
$A_g(2)$	428	439	443	$E_g(2)$	306	295	327
$A_g(3)$	474	457	458	$E_g(3)$	390	349	404
$A_g(4)$		533	501	$E_g(4)$	497	506	503
$A_g(5)$		597	604	$E_g(5)$	597	603	606
$A_g(6)$	612	618	622	$E_g(6)$	646	652	670

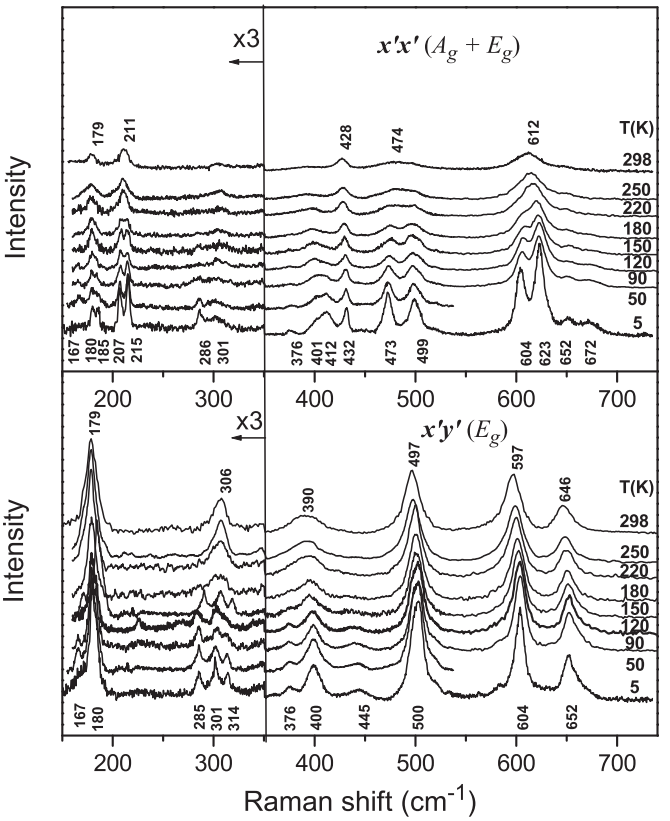

FIG. 3. Temperature-dependent $x'x'$ $(A_g + E_g)$ and $x'y'$ (E_g) spectra of $CaMn_7O_{12}$ between 5 and 298 K as obtained with 633-nm excitation.

B. Low-temperature spectra

In Fig. 3 are shown the variations in the Raman spectra of $CaMn_7O_{12}$ with lowering the temperature from 298 to 5 K. As expected the Raman bands become narrower and shift towards higher wave numbers, but no detectable anomalies directly related to the magnetic transition at $T_N \approx 90$ K are observed. What distinguishes this temperature behavior from that of other perovskitelike manganites, however, is the appearance below 200 K of additional weak spectral bands of A_g or E_g symmetry, thus significantly exceeding the number of Raman-allowed modes of the $R\bar{3}$ phase. These new spectral features are indicated by asterisks in Fig. 4 where the $x'x'$ and $x'y'$ spectra obtained with 633-, 515-, and 488-nm excitation at room (298 K) and low (8 K) temperatures are compared.

The appearance of new additional Raman modes coincides with the structural transformation resulting in incommensurate modulation of the atomic positions as evidenced by the detailed x-ray and neutron-diffraction experiments of Slawinski and co-workers [7–9]. Following their latest findings, unlike its parent $R\bar{3}$ structure, the symmetry of the superstructure due to modulation becomes $R3$ thus all Γ-point phonon modes become both Raman and infrared active. We can further speculate that due to the larger unit cell of the modulated structure some otherwise out-of-center phonon modes become Raman active. Except for the obvious correlation between structural modulation and new Raman band appearance,

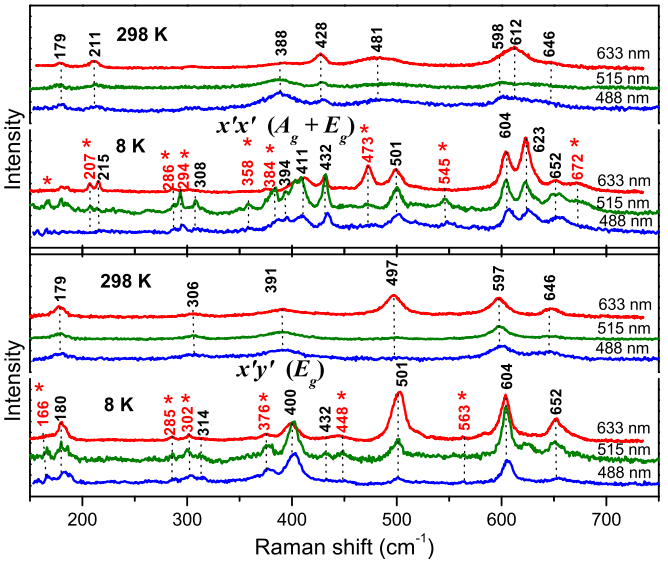

FIG. 4. (Color online) Comparison of the $x'x'$ $(A_g + E_g)$ and $x'y'$ (E_g) spectra obtained at 298 and 8 K with 633-, 515-, and 488-nm excitations. The additional spectral features in the 8-K spectra are indicated by asterisks.

however, it would be premature at this stage to make firm conclusions about their origins.

C. Effects of high-temperature trigonal-to-cubic transition

With increasing the temperature above 400 K $CaMn_7O_{12}$ enters a state of coexisting $R\bar{3}$ and $Im\bar{3}$ domains [16]. Above 440 K the structure is cubic, described by the $Im\bar{3}$ space group [10,16]. The description of the crystal symmetry by the $Im\bar{3}$ space group presupposes two basic assumptions: First, on the perovskite B position (here 8*c*) the mixture of nominally Mn^{3+} and Mn^{4+} ions is described by an averaged ion $Mn(B)^{3.25+}$ [assuming that the valence of the Mn(A) ions at the perovskite A positions (here 6*b*) is exactly 3+, (see Table IV)]; second, the six Mn(B)-O bonds are equal. In other words, in the cubic $Im\bar{3}$ one may expect either lack of ordering of JT octahedral distortions (i.e., they are frozen, but disordered, as in the rhombohedral $R\bar{3}c$ insulating phase of $LaMnO_3$) [17] or strong depression of the averaged JT distortion of $Mn^{3+}O_6$ octahedra (the difference between the lengths of the different Mn-O bonds) due to very fast electron transfer between Mn^{3+} and Mn^{4+} ions (as in the low-*T* metallic phase of $La_{0.7}Ca_{0.3}MnO_3$) [18]. The transport property studies [10,19] do show a resistivity drop of more than one order of magnitude at 440 K. However, both in low- and in high-temperature phases the electrical resistivity $\log_{10}\rho$ decreases linearly as temperature increases, which is typical for semiconductors.

TABLE IV. Wyckoff position of the atoms in the unit cell of the high-temperature phase $CaMn_7O_{12}$ ($Im\bar{3}$, No. 204, $Z = 2$). The irreducible representations of the Γ-point phonon modes are $\Gamma_{\text{Total}} = 2A_g + 2A_u + 2E_g + 2E_u + 4F_g + 12F_u$. Raman-active modes: $2A_g + 2E_g + 4F_g$; IR active modes: $11F_u$; acoustic modes $1F_u$; silent modes: $2A_u + 2E_u$ (Refs. [14,15]).

Atom	Wyckoff notation	Site Symmetry	Irreducible representations
Ca	2*a*	T_h	F_u
Mn(A)	6*b*	D_{2h}	$3F_u$
Mn(B)	8*c*	S_6	$A_u + E_u + 3F_u$
O	24*g*	C_s	$2A_g + 2E_g + 4F_g + A_u + E_u + 5F_u$

Raman spectroscopy is sensitive to the type of structural changes and can distinguish which kind of scenario takes place in the case of $CaMn_7O_{12}$. In the case of frozen disordered JT distortions (resulting in disordered oxygen sublattice) one expects activation of out-of-center phonon modes of mainly oxygen phonon branches, and the Raman spectrum will be dominated by broad bands roughly representing the smeared phonon density of states. In contrast, the transition to a metal state with strongly reduced JT distortions should result in a decrease in the phonon density-of-states band intensity while some zone-center modes may be observable. This problem is discussed in more detail in the example of mixed-valence manganites in Ref. [20]

The temperature dependence of the Raman spectra near the high-temperature structural transition is shown in Fig. 5. With increasing temperature in the rhombohedral phase the intensity of all lines strongly decreases. Above the $R\bar{3} \rightleftarrows Im\bar{3}$ transition all lines except these near 427 $cm^{-1}(A_g)$ and 600 $cm^{-1}(E_g)$ disappear. The changes are qualitatively the same as those observed near the structural phase transition between the low-temperature charge- and orbital-ordered phases and the high-temperature disordered phase of $La_{0.5}Ca_{0.5}MnO_3$ (there near 150 K) [21]. The intensity of the phonon

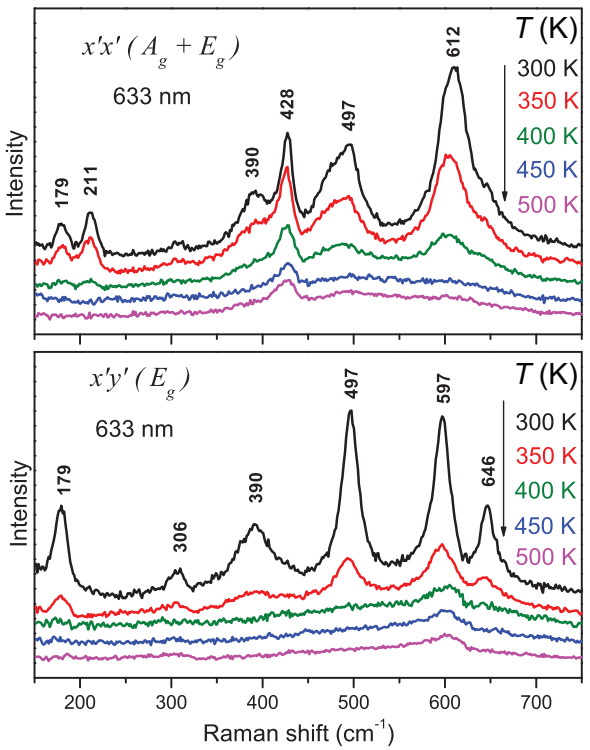

FIG. 5. (Color online) Variations between 300 and 500 K of the Raman spectra of $CaMn_7O_{12}$.

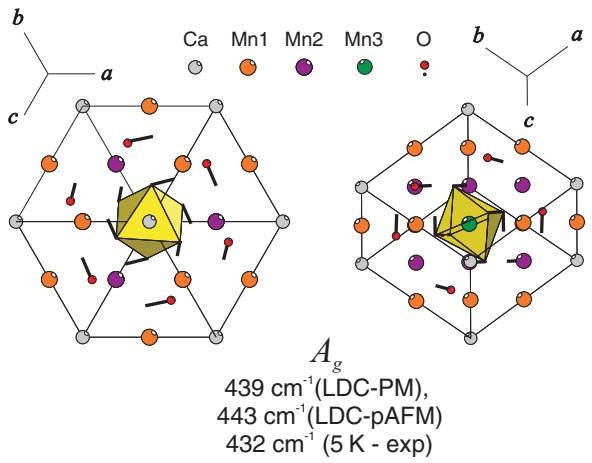

FIG. 6. (Color online) Eigenvectors corresponding to the A_g mode near 430 cm^{-1} seen in the left figure along the $[111]_c \| [111]_{rhomb}$ direction. In the cubic $Im\bar{3}$ phase Mn2 and Mn3 are equivalent.

density-of-states-like background in our case, however, is quite low, which is consistent with reduced dynamical Jahn-Teller distortions in the more conductive $Im\bar{3}$ phase due to enhanced $Mn^{3+} \rightleftarrows Mn^{4+}$ valence exchange.

In the high-temperature $Im\bar{3}$ phase of $CaMn_7O_{12}$ (as in its low-temperature phase) only the oxygen ions participate in the Raman-active modes: $2A_g + 2E_g + 4F_g$ (see Table IV). Comparing the $R\bar{3}$ and $Im\bar{3}$ structures one finds correlation between their Raman-active modes, namely, the four F_g modes of the cubic phase split into four A_g-E_g pairs in the rhombohedral phase. Taking into account that the rhombohedral deformation is small ($\alpha_{rhomb} = 90.4^\circ$), the frequency splitting between the modes of each pair should be small. Each A_g-E_g pair of lines must merge to one F_g line in the high-T phase. Due to the fact that their intensity quickly decreases as the temperature increases, only two of these pairs can be determined: A_g (612 cm^{-1}), E_g (597 cm^{-1}) and A_g (474 cm^{-1}), E_g (497 cm^{-1}).

D. A_g soft mode

We will speculate now about the origin of the A_g line near 430 cm^{-1}, still observed in the Raman spectra of the high-temperature phase. The $Im\bar{3}$ phase can be described using the Glazer notations, classifying the octahedral tilting in perovskites [22] as $(a^+a^+a^+)$, i.e., the $Mn(B)O_6$ octahedra are rotated as rigid units around the perovskite body diagonal [111]. In rotationally tilted perovskites, depending on the type of the tilting, one or two modes (the so-called soft modes) have the shape of the static tilt. The dependence of the frequency of the soft mode(s) on the tilt angle is simple proportionality and for manganites the proportionality coefficient is 22.8 cm^{-1}/deg [23]. In the $Im\bar{3}$ phase there is one mode of this type, and it is of A_g symmetry (librational vibration or rigid $Mn(B)O_6$ around the [111] axis). Using the structural data from Ref. [19], the octahedral tilting angle in the cubic $CaMn_7O_{12}$ is quite large (23.8°). It is not clear if the proportionality dependence derived in Ref. [23] can still be used for such large angles and whether the approximation is valid for having two types of ions of different valences (Ca^{2+} and Mn^{3+}) at the A positions. The predicted frequency is quite high −543 cm^{-1}, but in any case the expected frequency should be above 400 cm^{-1}. Based on the fact that the line near 430 cm^{-1} in the spectra of $CaMn_7O_{12}$ remains of A_g symmetry in the $Im\bar{3}$ phase as well as the lattice-dynamical modeling confirms (see Fig. 6) that it corresponds to $Mn(B)O_6$ rotations around the [111] cubic diagonal, we can with great certainty assign it to the A_g soft mode.

IV. CONCLUSIONS

In conclusion, this paper reports on the polarized Raman spectra of $CaMn_7O_{12}$ in a broad temperature range covering the crystallographic, ferroelectric, and magnetic transitions. Ten out of the total twelve Raman active $6A_g + 6E_g$ modes of the trigonal $R\bar{3}$ phase have been identified and have been assigned to definite atomic motions in close comparison to results of lattice-dynamics modeling. With the decrease in the temperature below 250 K some Raman bands split, and additional spectral features, not expected for the $R\bar{3}$ structure, arise well above the magnetic transitions near 90 and 50 K. Their appearance correlates with the imposition of incommensurate structural modulation revealed by recent x-ray and neutron-diffraction studies. As temperature increases above RT the intensity of the Raman lines strongly decreases and entering the high-temperature $Im\bar{3}$ phase the spectrum transforms its shape to that expected for a conducting state with disordered and strongly suppressed Jahn-Teller distortions.

ACKNOWLEDGMENTS

This work was supported by the State of Texas through the Texas Center for Superconductivity at the University of Houston (TcSUH). The work of M.M.G. was supported by the project INERA (Grant No. GA 316309) of the Seventh Framework Program of the European Union. M.V.A. thanks the Brazilian agency CAPES (Project No. BEX 7607-13-0) for financial support.

[1] B. Bochu, J. L. Buevoz, J. Chenavas, A. Collomb, J. C. Joubert, and M. Marezio, Solid State Commun. **36**, 133 (1980).
[2] R. Przeniosło, I. Sosnowska, D. Hohlwein, T. Hauß, and I. O. Troyanchuk, Solid State Commun. **111**, 687 (1999).
[3] R. D. Johnson, L. C. Chapon, D. D. Khalyavin, P. Manuel, P. G. Radaelli, and C. Martin, Phys. Rev. Lett. **108**, 067201 (2012).
[4] M. Sánchez-Andújar, S. Yáñez-Vilar, N. Biskup, S. Castro-García, J. Mira, J. Rivas, and M. A. Señarís-Rodríguez, J. Magn. Magn. Mater. **321**, 1739 (2009).
[5] X. Z. Lu, M.-H. Whangbo, S. Dong, X. G. Gong, and H. J. Xiang, Phys. Rev. Lett. **108**, 187204 (2012).

[6] J. T. Zhang, X. M. Lu, J. Zhou, H. Sun, F. Z. Huang, and J. S. Zhu, Phys. Rev. B **87**, 075127 (2013).
[7] W. Slawinski, R. Przenioslo, I. Sosnowska, M. Bieringer, I. Margiolaki, and E. Suard, Acta Cryst. B **65**, 535 (2009).
[8] W. Sławiński, R. Przenioslo, I. Sosnowska, and M. Bieringer, J. Phys.: Condens. Matter **22**, 186001 (2010).
[9] W. Slawinski, R. Przenioslo, I. Sosnowska, and V. Petrícek, Acta Cryst. B **68**, 240 (2012).
[10] I. O. Troyanchuk and A. N. Chobot, Crystallogr. Rep. **42**, 983 (1997) [Kristallografiya **42**, 1058 (1997)].
[11] Agilent, CRYSALIS PRO (version 1.171.35.15). 9 (Agilent Technologies Ltd, Yarnton, U.K., 2010).
[12] G. M. Sheldrick, Acta. Cryst. A **64**, 112 (2008).
[13] P. Giannozzi, S. Baroni, N. Bonini, M. Calandra, R. Car, C. Cavazzoni, D. Ceresoli, G. L. Chiarotti, M. Cococcioni, I. Dabo, A. Dal Corso, S. de Gironcoli, S. Fabris, G. Fratesi, R. Gebauer, U. Gerstmann, C. Gougoussis, A. Kokalj, M. Lazzeri, L. Martin-Samos, N. Marzari, F. Mauri, R. Mazzarello, S. Paolini, A. Pasquarello, L. Paulatto, C. Sbraccia, S. Scandolo, G. Sclauzero, A. P. Seitsonen, A. Smogunov, P. Umari, and R. M. Wentzcovitch, J. Phys.: Condens. Matter **21**, 395502 (2009).
[14] M. I. Aroyo, J. M. Perez-Mato, C. Capillas, E. Kroumova, S. Ivantchev, G. Madariaga, A. Kirov, and H. Wondratschek, Z. Krist. **221**, 15 (2006).
[15] M. I. Aroyo, A. Kirov, C. Capillas, J. M. Perez-Mato, and H. Wondratschek, Acta Cryst. A **62**, 115 (2006).
[16] R. Przenioslo, I. Sosnowska, E. Suard, A. Hewat, A. N. Hewat, and A. N. Fitch, J. Phys.: Condens. Matter **14**, 5747 (2002).
[17] Q. Huang, A. Santoro, J. W. Lynn, R. W. Erwin, J. A. Borchers, J. L. Peng, and R. L. Greene, Phys. Rev. B **55**, 14987 (1997).
[18] A. P. Ramirez, J. Phys.: Condens. Matter **9**, 8171 (1997).
[19] I. O. Troyanchuk, L. S. Lobanovsky, N. V. Kasper, M. Hervieu, A. Maignan, C. Michel, H. Szymczak, and A. Szewczyk, Phys. Rev. B **58**, 14903 (1998).
[20] M. N. Iliev, M. V. Abrashev, V. N. Popov, and V. G. Hadjiev, Phys. Rev. B **67**, 212301 (2003).
[21] M. V. Abrashev, J. Bäckström, L. Börjesson, M. Pissas, N. Kolev, and M. N. Iliev, Phys. Rev. B **64**, 144429 (2001).
[22] A. M. Glazer, Acta Cryst. B **28**, 3384 (1972).
[23] N. D. Todorov, M. V. Abrashev, and V. G. Ivanov, J. Phys.: Condens. Matter **24**, 175404 (2012).